ACS OMEGA

http://pubs.acs.org/journal/acsodf

Article

Electrochemical and Surface Characterization Study on the Corrosion Inhibition of Mild Steel 1030 by the Cationic Surfactant Cetrimonium Trans-4-hydroxy-cinnamate

Jhonatan Soto Puelles, Mahdi Ghorbani, Ruhamah Yunis, Laura L. Machuca, Herman Terryn, Maria Forsyth,* and Anthony E. Somers*

Cite This: *ACS Omega* 2021, 6, 1941−1952

Read Online

ACCESS | Metrics & More | Article Recommendations | Supporting Information

ABSTRACT: Effective corrosion inhibition of mild steel 1030 at 0.01 M NaCl concentration was achieved by the use of the nontoxic surfactant salt cetrimonium trans-4-hydroxy-cinnamate (CTA-4OHcinn). Polarization analysis on the steel samples immersed for 24 h in the control and CTA-4OHcinn-containing solutions shows the development of a passivation potential that is more obvious at higher inhibitor concentrations along with a maximum inhibition efficiency of 97.8%. Electrochemical impedance spectroscopy (EIS) pinpoints the effect of the inhibitor on the corroding regions of the metal surface, showing an increase in the local electric resistance and conversely a decrease in the local capacitance, which indicates that the charge transfer in the corroding regions is being hindered by a deposition process. This is consistent with scanning electron microscopy (SEM) images, showing the presence of a porous oxide matrix that fills localized corrosion sites on the metal surface after 24 h of immersion in a 0.01 M NaCl + 10 mM inhibitor solution. Additionally, SEM analysis also shows the formation of an organic film surrounding the defects that is able to shield chloride attack. As a result of diffusion of chloride from the defects below the protective film, filiform corrosion can be seen. Time-resolved impedance analysis over the first 120 min of immersion in the control and inhibitor solution shows that significant inhibitor protection does not take place immediately and there is a lag phase in the first 50 min of immersion, suggesting that early localized corrosion drives further adsorption of inhibitor micelles on the metal surface. This is in agreement with X-ray photoelectron spectroscopy (XPS) analysis, which indicates a complete surface coverage over the first 2 h of immersion in a concentrated inhibitor solution. XPS also shows the heterogeneity of the film, where some parts are poorly covered, revealing the underlying surface containing iron.

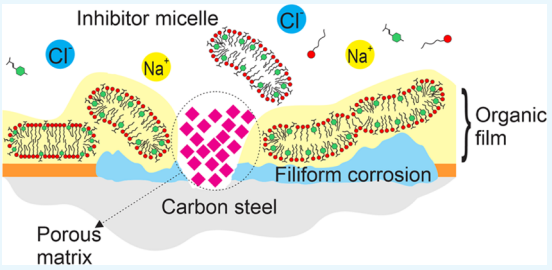

INTRODUCTION

The use of organic molecules with carboxylate moieties as corrosion inhibitors, such as cinnamate-based compounds, has been described elsewhere. It was proposed that they could be used as potential candidates for the substitution of toxic inhibitors such as hexavalent chromium because of their ability to form coordinate bonds with metal atoms such as iron and aluminum on the solid−electrolyte interface.[1,2] Combinations of these organic anions with rare-earth cations, which have also shown promising results by themselves as corrosion inhibitors,[3] have led to effective synergy mechanisms maximizing the metal protection. As shown by Behrouzvaziri et al., lanthanum 4-hydroxycinnamate [$La(4OHcin)_3$] inhibits mild steel corrosion in NaCl solutions by forming a protective film on the metal surface with nodular particles rich in La and Fe.[4,5] It was proposed that, at a first stage, localized corrosion occurs at defective zones of the metal surface, releasing iron ions that react with the ionic species of the solution, promoting the formation of the deposits on the surface. In addition, the hydroxyl species formed in the cathodic regions react with the rare-earth cations, forming insoluble species contributing to the film formation.[6] The presence of a bimetallic film between lanthanum species and the underlying iron atoms from the steel surface was supported by Fourier transform infrared (FTIR) measurements and impedance spectroscopy that showed an increase in the local electric resistance at the interface as a result of the inhibitor interaction.[7−9] Along with the carboxylate moiety, the position of the hydroxyl group in hydroxy-cinnamate species has been shown to play an important role in the mechanism of inhibition. Nam et al. showed that cerium 2-hydroxy-cinnamate performs better than cerium 4-hydroxycinnamate, inhibiting the corrosion of steel in NaCl solution. It was hypothesized that the hydroxyl groups interact with the metal surface by hydrogen bonding, and in

Received: September 27, 2020
Accepted: November 16, 2020
Published: January 8, 2021

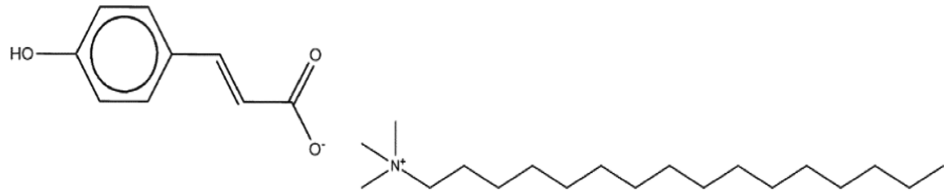

Figure 1. Molecular structure of CTA-4OHcinn.

the case of the ortho substitution (2-OH-cin), the aromatic ring is shielded, preventing further interactions and forming a uniform film compared to the ortho substitution (4-OH), where a multilayered film with cracks was observed by scanning electron microscopy (SEM) analysis.[10] In addition to lanthanum and cerium counterions for cinnamate compounds, other rare-earth elements have also been tested; e.g., praseodymium 4-hydroxycinnamate, $Pr(4OHCin)_3$, was reported to inhibit cathodic and anodic reactions simultaneously on mild steel immersed in saturated CO_2 saline solutions by forming a densely packed crystalline film.[11] Similarly, yttrium 4-nitrocinnamate, $Y(NO_2Cin)_3$, showed good corrosion inhibition properties of mild steel in saline solutions, where surface analysis indicated the $Y(NO_2Cin)_3$ hydrolysis resulting in precipitates and the development of a protective layer.[12]

Contrasting the well-documented synergy mechanism between rare-earth cations and cinnamate-based compounds, the use of organic cations has been poorly mentioned in the literature. Chong et al. replaced the inert sodium counterion of 4-hydroxycinnamate by the active inhibitor cation 2-methylimidazolinium.[13] Synergy was confirmed by showing that the new organic salt 2-methylimidazolinium 4-OH cinnamate performed better when compared to sodium cinnamate alone and 2-methylimidazolinium bromide alone, inhibiting corrosion of mild steel in saline solutions at acid, neutral, and basic pH.

Following this work, the authors hypothesized that by including a surface-active counterion along with the 4-OH cinnamate, it might be possible to develop a multifunctional inhibitor compound that, in addition to inhibiting corrosion on mild steel, could also disrupt bacterial membranes, thereby inhibiting biofilm formation. The cetrimonium cation chosen in the work reported here is based on the work of Seter et al., who reported a synergistic effect between this surface-active species and nalidixate anions, inhibiting biofilm formation and corrosion of mild steel simultaneously.[14] The new inhibitor compound reported in this work is cetrimonium 4-OH cinnamate, CTA-4OHcinn (Figure 1).

Interestingly, although the literature on corrosion research shows no studies regarding the behavior of surface-active compounds and aromatic counterions in solution, which is important in determining performance, this problem has been addressed by soft matter and medical research fields showing the potential of these amphiphilic substances to encapsulate hydrophobic drugs and increase their apparent solubility.[15,16] For example, when methyl-salicylic acid is added to a cetrimonium bromide solution, along with a transition from spherical to wormlike micelles, there is a sharp increase in the system viscosity and an excess concentration of the aromatic counterion compared to its normal solubility.[17] We confirm some sort of micellization mechanism between the ionic species in the inhibitor of interest in this work, based on the NMR studies from Ghorbani et al.[18]

In the present work, we study the potential of the organic compound CTA-4OHcinn in inhibiting corrosion of mild steel in a saline solution by performing electrochemical and surface characterization techniques. Using potentiodynamic polarization, the electrochemical nature and passivating properties of CTA-4OHcinn are elucidated. In addition, impedance analysis allows us to identify the local capacitive and resistive contributions at the solid−electrolyte interface. The morphology of the modified surface is analyzed by SEM/energy dispersive X-ray spectroscopy (EDS) imaging. Finally, the dynamics and composition of the film are studied by carrying out time-resolved electrochemical impedance spectroscopy (EIS) analysis along with X-ray photoelectron spectroscopy (XPS) on the metal surface at different immersion times and inhibitor concentrations.

METHODOLOGY

In this work, the surfactant-based ionic liquid cetrimonium trans-4-hydroxy-cinnamate, CTA-4OHcinn, was investigated as a corrosion inhibitor compound. It was synthesized using *p*-coumaric acid and cetrimonium bromide as precursors, following the silver route as detailed in the work of Ghorbani et al.[18] As shown in Figure 1, it consists of a cetrimonium cation and a coumarate anion.

Preparation of Steel Coupons. Mild steel 1030 cylindrical coupons with a circular area of 0.786 cm^2 (1 cm diameter) were used in this work, whose atomic composition based on glow-discharge optical emission spectroscopy (GDOES) is 98.27% Fe, 0.35% C, 0.21% Si, 0.74% Mn, 0.17% Cr, and others 0.26%. Prior to the electrochemical and surface characterization experiments, the coupons were embedded in epoxy resin, leaving exposed a circular area. The exposed areas were finished by grinding with 240, 800, and 1200 grit silicon carbide paper using a mechanical polisher with a continuous flow of distilled water. The water excess was removed with a nitrogen drying gun, and the samples were rested in a silica gel desiccator for 24 h prior to the tests.

Preparation of Control and Inhibitor Solutions. All of the solutions contained 0.01 M NaCl, and the concentrations of CTA-4OHcinn were 0 mM (for the control test), 2.5, 5, and 10 mM. As the solubilization of CTA-4OHcinn was slow, the temperature was increased to 40 °C with a magnetic stirrer, to accelerate the process. Also, the inhibitor solutions initially had an acid pH between 5 and 5.5, which was readjusted to pH 7 using a diluted NaOH solution. Finally, the solutions were stored at a temperature of 20 °C.

Optical Microscopy and SEM. The optical and SEM imagings were carried out in a Leica DMi8 and a JEOL IT300, respectively. The same SEM was used for the energy-dispersive spectroscopy analysis using an Oxford X-Max 50 mm^2 detector and Oxford Aztec software.

Electrochemical Techniques. Potentiodynamic polarization tests were carried out in a BioLogic VMP3 potentiostat at the same concentrations used for the immersion tests, with

https://dx.doi.org/10.1021/acsomega.0c04733
ACS Omega 2021, 6, 1941−1952

open circuit potential offsets of 150 and 300 mV for the cathodic and anodic potentials, respectively. For the control test at 0.01 M NaCl, the cathodic branch had a 60 mV offset. Two repeats were done for each concentration, spanning from the cathodic to the anodic potential at each test. The data analysis was done in EC Lab 11.27 software, and for the Tafel extrapolation, an offset of ±25 mV from the open circuit potential was considered with a width of 10 mV for each regression line.

For the electrochemical impedance spectroscopy test, a low current VMP channel connected to the Biologic potentiostat was used. The perturbation signal had a voltage amplitude of 10 mV, and for the analysis, in the first 2 h of immersion, the frequency range was limited to a range of 200 kHz−100 mHz. A final EIS measurement was taken after 24 h of immersion at the same frequency range. The solution concentrations were the same as specified for the polarization and immersion experiments, and two repeats were carried out.

XPS Analysis. X-ray photoelectron spectroscopy (XPS) was carried out on a Kratos Nova instrument using an Al Kα energy source at 1486.6 eV. The scans were conducted using an anode voltage of 15 kV and a current of 10 mA. A pass energy of 160 eV was used for survey scans and 20 eV for high-resolution scans. Casa XPS software was used for the postprocessing of the data. For calibration of the spectra, charge correction of the C 1s peak at 284.8 eV was used as a reference, and the deconvolution analysis was done with a Shirley background. Based on results from the EIS measurements, samples were immersed for 15 min, 45 min, 2 h, and 24 h in 0.01 M NaCl plus 10 mM cet-trans-4OH-cinn solution. Also, a control sample was prepared by 45 minutes immersion in 0.01 M NaCl solution.

RESULTS AND DISCUSSION

Figure 2 shows the representative polarization curves for mild steel after 24 h of immersion in different CTA-4OHcinn

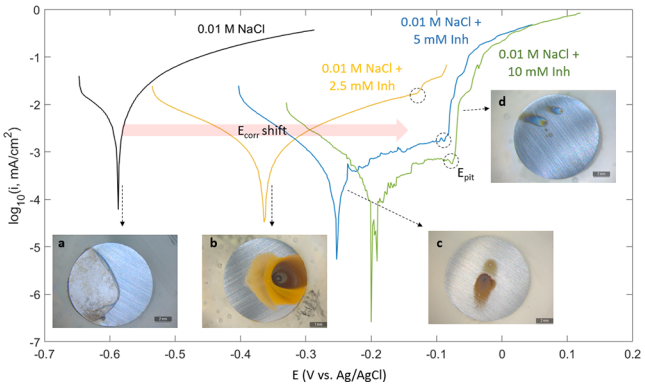

Figure 2. Potentiodynamic polarization of mild steel immersed for 24 h in 0.01 M NaCl control (black line) and various concentrations of CTA-4OHcinn with their respective images.

concentrations; their respective replicas can be found in the Supporting Information. As the concentration increases, the corrosion potential E_{corr} shifts toward more positive values due to a decrease in the anodic curve (the right branch), which is characteristic of an anodic inhibitor. At higher potentials, the anodic curves for mild steel immersed in CTA-4OHcinn present an inflection point (dashed circles) where the current rises sharply, defined as the pitting potential, E_{pit}. It was noticed that E_{pit} occurs at lower currents as the inhibitor concentration increases, indicating the development of a passivating film as a result of the inhibitor addition. The anodic shift of E_{pit} implies that the passivation layer that forms is more stable and breakdown occurs at a higher anodic voltage. This is an indication that the protection improves at higher inhibitor concentrations. Also, the E_{corr} for the sample immersed in the 10 mM inhibitor solution is not clearly defined and oscillates around −0.2 V, which could indicate a metastable pitting process.[19]

Assuming a linear relationship between the logarithm of current density and potential near E_{corr}, the corrosion current i_{corr} was extracted by adjusting the experimental data to the Tafel equation (eq 1).[20] The estimated i_{corr} values for each polarization curve, with its respective deviation, along with the E_{pit} and inhibition efficiency η, are shown in Table 1. Equation

Table 1. Parameters Extracted from the Polarization Curves for Mild Steel Immersed at Different CTA-4OHcinn Concentrations after 24 h Immersion

CTA-4OHcinn concentration, mM	E_{corr}, mV	i_{corr}, μA/cm^2	E_{pit}, mV	η, %
0	−587	2.19 ± 0.37		
2.5	−361	0.24 ± 0.08	−128	89
5	−250	0.11 ± 0.001	−82	95
10	−192	0.05 ± 0.001	−72	98

1 shows the formula for the inhibition efficiency, where i_{corr} represents the corrosion current of the sample immersed in the control solution; i_{corr_i} is the corrosion current for the sample immersed in the inhibitor solution, and η is the inhibition efficiency in percentage. This is commonly used in the corrosion inhibitor field for comparison of efficacy of an inhibitor system.

$$\eta = 100 \times \left(\frac{i_{corr} - i_{corr\_i}}{i_{corr}} \right) \quad (1)$$

The analysis shows that the inhibition efficiency approaches 100% as the CTA-4OHcinn concentration increases. This is in agreement with the inset images b−d in Figure 2, showing less oxide deposited on the steel surface with the increase in inhibitor concentration.

Figure 3 shows the Nyquist plot for the sample immersed for 2 h in control and inhibitor solutions. The magnification in the inset image reveals that each Nyquist curve is formed by two capacitive arcs. The small arc corresponds to a high-frequency range between 200 and 4 kHz and the large semicircle to a low-frequency range between 4 kHz and 100 mHz. The addition of the inhibitor has a significant effect on the lower frequency impedance, causing an increase in the diameter of the larger arc, which is related to the development of a capacitive surface film.[21] This event could be linked to a deposition process of an insoluble compound on these localized corrosion regions,[22] and it is consistent with the polarization experiments that show the affinity of the inhibitor to hinder anodic reactions. Previous studies on rare-earth 4-OH cinnamates suggest that defective zones on the steel surface possess a high reactivity and promote complexation of the cinnamate species.[6] It is clear that the inhibitor not only contributes to the resistive behavior of the interface but also affects its capacitance, which is reflected in the higher values of the imaginary impedance for the samples immersed in

https://dx.doi.org/10.1021/acsomega.0c04733
ACS Omega 2021, 6, 1941−1952

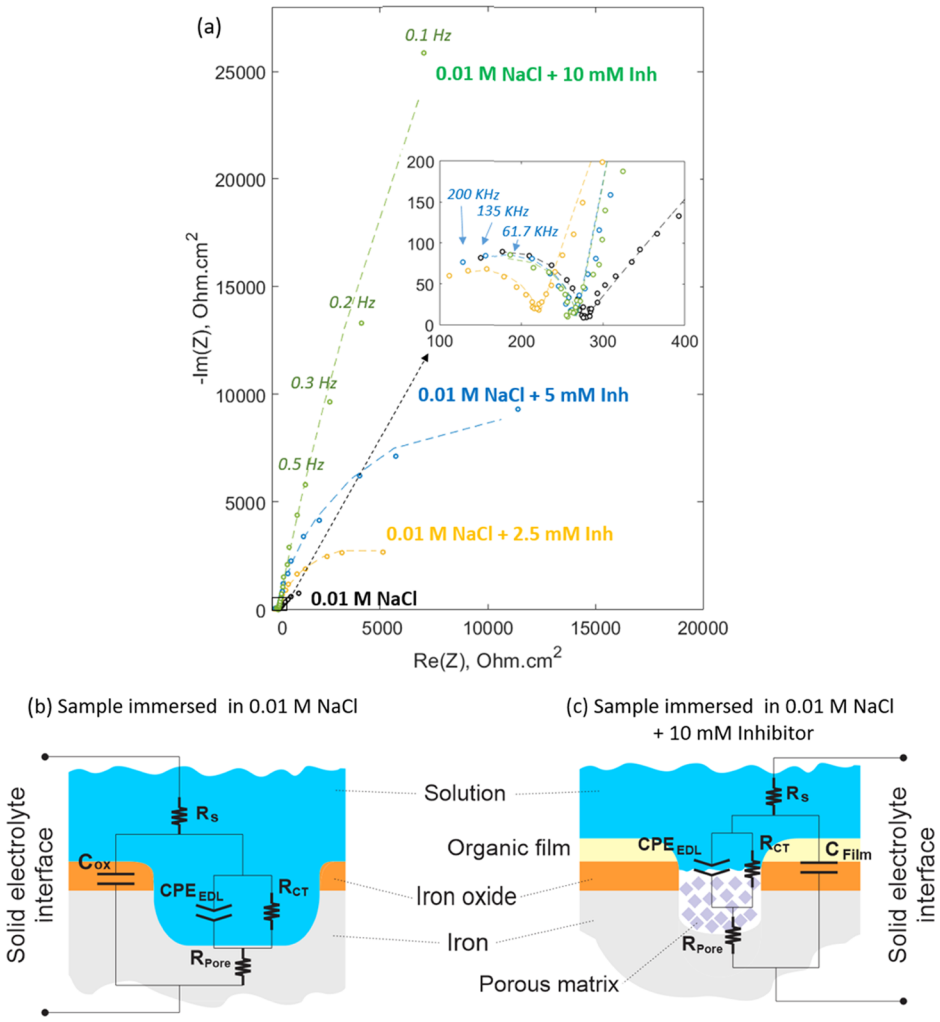

Figure 3. Nyquist plot for mild steel immersed for 2 h in different CTA-4OHcinn concentrations. The dashed lines correspond to the predicted values by their respective equivalent circuit model (a). Proposed equivalent circuit models for the sample immersed in 0.01 M NaCl control solution (b) and the sample immersed in 0.01 M NaCl + 10 mM inhibitor solution (c).

Table 2. Fitting Parameters for the Proposed Equivalent Circuit Model at Different Inhibitor Concentrations after 2 and 24 h of Immersion (Values Enclosed in Parenthesis Correspond to 24 h of Immersion)

	R_s (Ω cm^2)	$C_{ox/film}$ (nF cm^{-2})	R_{pore} (Ω cm^2)	CPE$_{EDL}$ (μF $s^{\alpha-1}$)	α	R_{CT} (kΩ cm^2)	S^2
control	117.9 (123.7)	26.61 (15.89)	228.2 (223.5)	751.0 (756.2)	0.578 (0.615)	6.707 (2.688)	0.014 (0.011)
0.01 mM NaCl + 2.5 mM Inh	109.9 (121.3)	100.3 (75.39)	170.5 (165.6)	114.4 (101.5)	0.816 (0.820)	9.646 (16.137)	0.028 (0.069)
0.01 mM NaCl + 5 mM Inh	119.3 (155.8)	35.89 (35.99)	220.3 (185)	0.0576 (0.0433)	0.886 (0.907)	26.927 (141.612)	0.029 (0.032)
0.01 mM NaCl + 10 mM Inh	132.6 (115.4)	18.89 (12.13)	207.4 (225.7)	0.0473 (0.0327)	0.881 (0.901)	377.945 (21.03e15)	0.047 (0.206)

inhibitor solutions. As a consequence of the inverse relationship between capacitance and imaginary impedance, the inhibitor addition decreases the low-frequency capacitance, reflecting a film formation process at the interface.[12]

To further understand the charge-transfer mechanism at the interface, equivalent circuit models were derived from the EIS spectra. The proposed models are constrained by SEM and XPS surface analyses, which show the presence of an organic film along with a porous matrix in the localized corrosion regions for the sample immersed in the inhibitor solution. A similar model was considered for the sample immersed in 0.01 M NaCl control solution because it was observed that the shape of the Nyquist plot was not affected by the inhibitor concentration; i.e., all of the plots presented two arcs (Figure 3a). The models are presented in Figure 3b,c, where R_s represents the solution resistance, R_{CT} is the charge-transfer resistance, R_{pore} is the pore resistance, C_{ox} is the capacitance of the oxide layer, C_{layer} is the capacitance of the inhibitor layer, and CPE$_{ELD}$ is the constant phase element for the electric double layer. The use of a constant phase element instead of a capacitor component at the pore interface is due to the surface heterogeneity that produces a low-frequency defective semicircle.[23] It is also noticed that R_{pore} represents an exposed metal surface as a result of chloride attack for the control (Figure 3b), while for the sample immersed in the inhibitor solution, it is related to the resistance of the material deposited on the defective zone (Figure 3c).

Table 2 shows the parameters resulting from fitting the equivalent circuit model to the experimental data. The last column corresponds to the standard deviation between the

https://dx.doi.org/10.1021/acsomega.0c04733
ACS Omega 2021, 6, 1941−1952

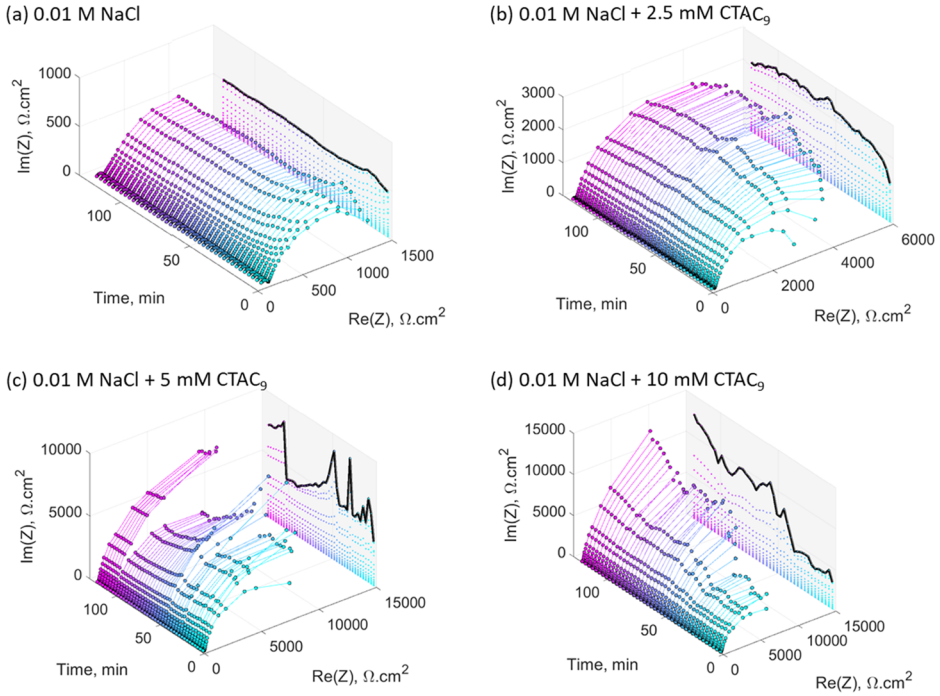

Figure 4. Time evolution of the Nyquist plot for mild steel over the first 2 h of immersion in 0.01 M NaCl (a), 0.01 M NaCl + 2.5 mM CTA-4OHcinn (b), 0.01 M NaCl + 5 mM CTA-4OHcinn (c), and 0.01 M NaCl + 10 mM CTA-4OHcinn (d).

experimental data and the objective function that confirms that the fitting was adequate for all of the scenarios with the error not greater than unity. The values inside the parenthesis correspond to the fitting parameters for EIS data after 24 h of immersion, which will be discussed in the next section. The effect of the inhibitor on the solution resistance, R_s, is not clear; although it shows an increasing trend with the inhibitor concentration, the control test still possesses a greater R_s compared to the sample immersed in the 2.5 mM inhibitor solution. In the Nyquist diagram, this resistance corresponds to the intersection between the real axis and the extrapolation of the higher-frequency loop (from the left side). As can be seen in Figure 3a, in the four scenarios, such an intersection would not vary considerably.

The oxide/film capacitance also does not follow a clear trend. It is noticed that at 2.5 mM, this parameter increases sharply by one order of magnitude from 26.61 to 100.3 nF cm^{-2}; this can be related to the oxide deposition on the metal surface. A higher capacitance implies a major surface coverage, and it is consistent with snapshot b of Figure 2, where the mild steel sample immersed in the 2.5 mM inhibitor solution shows the highest deposition as a result of the inhibitor interaction, compared to the other three cases. At 5 and 10 mM inhibitor concentrations, $C_{ox/film}$ does not differ considerably compared to the control test and even decreases from 26.61 to 18.89 nF cm^{-2}. This suggests that, although the inhibitor is depositing across the metal surface, as shown by EDS and XPS analyses, the biggest effect happens at the interface of the anodic regions, which is consistent with the polarization data. The smaller arcs in the Nyquist plot do not vary considerably in the four cases (Figure 3) and explain why $C_{ox/film}$ is within the same order of magnitude except for the 2.5 mM inhibitor concentration. An opposite trend was reported by Nam et al. studying the CO_2 corrosion inhibition of mild steel with praseodymium 4-hydroxycinnamate, where the high-frequency capacitive arc was larger than the low-frequency arc when the inhibitor interacted with mild steel. This effect was ascribed to the additional surface film deposited on the cathodic zones due to the hydrolysis of the rare-earth ions.[11] The similarity of the pore resistances, R_{pore}, in the four cases suggests that this parameter could be representing the same material, i.e., the exposed iron in the case of the sample immersed in the control solution and the iron beneath the porous matrix in the case of the sample immersed in the inhibitor solution.

It is observed that the constant phase element of the electric double layer, CPE_{EDL} (ideally represented by a capacitor), decreases in an inverse relation with the inhibitor concentration by four orders of magnitude. This is related to a deposition process or a decrease in the local dielectric constant.[8,24,25] It is also consistent with the SEM images of the steel surface after inhibitor interaction that shows that the defective zone is filled with a porous oxide matrix (Figure 7c). The same film formation process causes an increase in the charge-transfer resistance, R_{CT}, by two orders of magnitude of the steel sample immersed in the inhibitor solution. This parameter is related to the electric resistance at the solid–electrolyte interface on the localized corrosion regions.[26] Polarization tests also support this result, showing the affinity of the inhibitor for hindering anodic reactions. The parameter α that accounts for the heterogeneity on the metal surface[23] in the impedance formula of the constant phase element, $Z = 1/C^{\alpha}$, increases from 0.5, in the case of the control test, to 0.8, for all of the inhibitor solutions. This parameter may be related to the roughness of the surface, and as observed in SEM images (Figure 7a), the control test presented extensive corrosion where most of the surface was affected, which corresponds to a higher roughness compared to the samples immersed in all inhibitor solutions.

Figure 4 shows the evolution of the Nyquist plots over the first 2 h of immersion, with scans performed every 3 min. The projected line represents the maximum height of each semicircle (i.e., the maximum imaginary impedance, Im|Z|,

https://dx.doi.org/10.1021/acsomega.0c04733
ACS Omega 2021, 6, 1941−1952

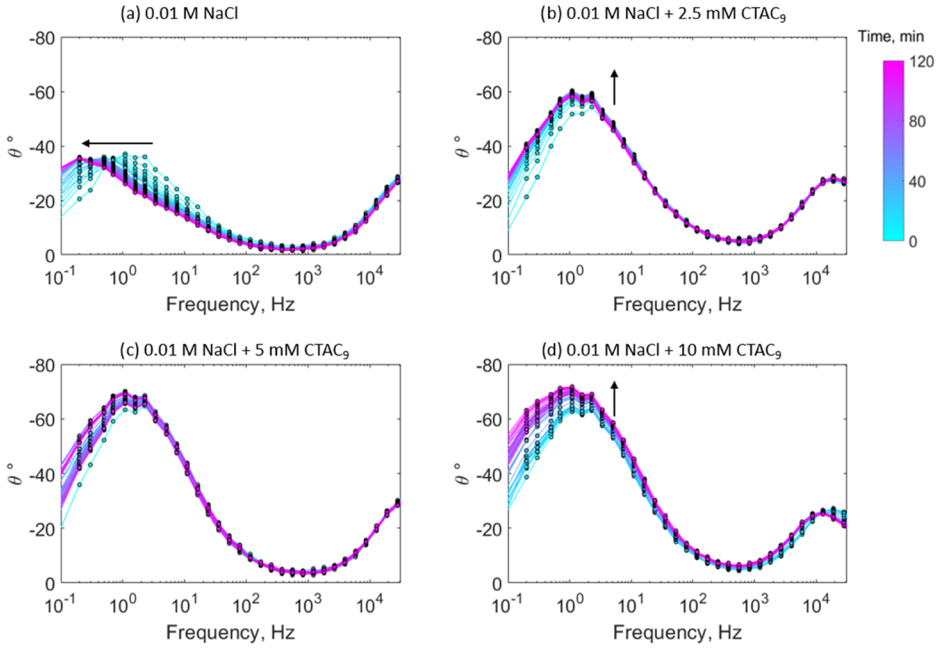

Figure 5. Time evolution of the phase angle diagram for mild steel immersed for 2 h in different CTA-4OHcinn concentrations. Each color represents a determined time based on the color bar at the right.

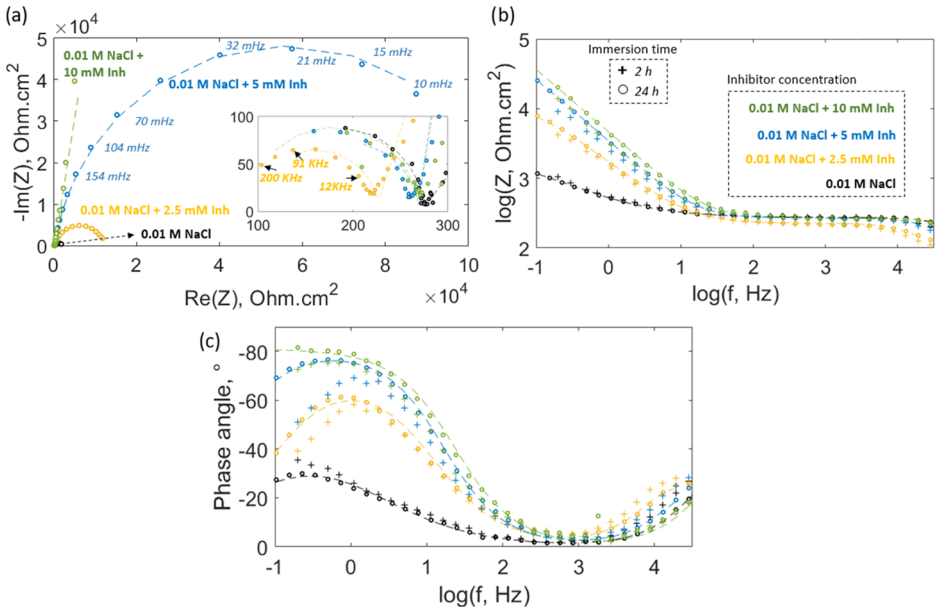

Figure 6. Nyquist diagram for the sample after 24 h of immersion at different inhibitor concentrations; the dashed line represents the fitting with their respective equivalent circuit model (a). Impedance and phase angle Bode plot for the sample immersed for 24 h (circles) and 2 h ("+" sign) in different inhibitor concentrations; the dashed line also corresponds to the fitting (b, c).

which is measured at lower frequencies). In the case of the sample immersed in the 0.01 M NaCl control solution, the projected line shows a constant trend with time and is lower than all of the inhibitor containing solutions, indicating a constant capacitance at the interface of the defective regions on the metal surface. This is consistent with its respective image, showing no significant attachment of the oxide material on the surface (Figure 2a). For the sample immersed in the 2.5 mM inhibitor solution, the low-frequency impedance rises smoothly over the first 50 min (based on the projected line) and after that follows a constant trend as shown in Figure 4b. The initial increase in impedance might be related to the oxide deposition observed on the metal surface (Figure 2b). In the case of the sample immersed in the 5 mM inhibitor solution (Figure 4c), the projected line shows an oscillating behavior, which might be related to a competitive process between localized corrosion and film formation. Finally, the sample immersed in the 10 mM inhibitor solution (Figure 4c) presents an initial low-impedance window (in the low-frequency region) in the first 50 min of immersion, where the projected line is approximately constant. The same behavior was observed in the respective replica attached in the Supporting Information. The initial adsorption of inhibitor molecules on the surface could be attributed to a change in the interface environment due to

https://dx.doi.org/10.1021/acsomega.0c04733
ACS Omega 2021, 6, 1941−1952

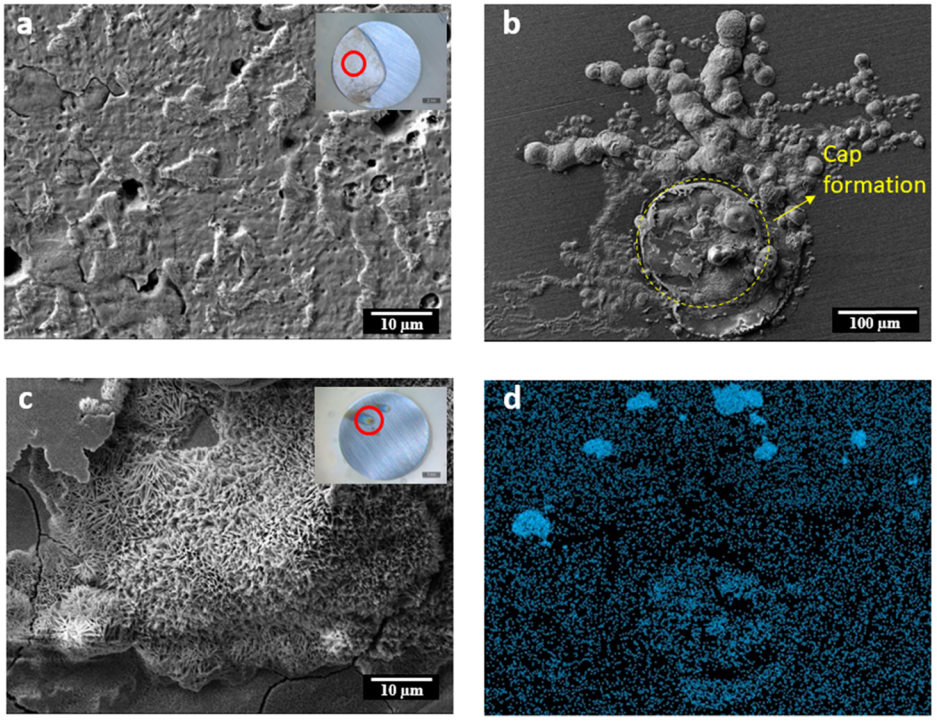

Figure 7. SEM images for mild steel immersed for 24 h in the control 0.01 M NaCl solution (a) and immersed in the 0.01 M NaCl + 10 mM CTA-4OHcinn inhibitor solution with its respective chloride EDS map (b, d); higher magnification of image b (c).

early localized corrosion. This is consistent with the work of Blin et al. that identified the formation of coumarate complexes on the steel surface through attenuated total reflection (ATR)-FTIR.[9] In addition, the presence of inhibitor micelles should be considered, as reported by Ghorbani et al., which are susceptible to changes in their morphology due to disruptions in their environment.[18] For example, early localized corrosion could increase the ionic strength at the interface, which in turn would promote the coalescence of the micelles.[27] The projected line also shows a sharp increase after the low-impedance window, which could be linked to the deposition of the insoluble compound on the defective regions of the metal surface.

Figure 6 shows the evolution of the phase angle over 2 h for these samples immersed at different inhibitor concentrations. In all cases, the maximum phase angle peak is found in the low-frequency range, below 10 Hz. The control test shows a shift of its maximum phase angle peak toward lower frequencies with time (as shown by the arrow in Figure 5a). Duan et al. related this lower frequency shift to an increase in the area of the metal exposed to a corrosive environment.[28] In the case of the sample immersed in 2.5 and 10 mM inhibitor solutions, the maximum peak increases with time and presents no significant shift with frequency (Figure 5b,d, respectively). Ye et al. related the increase and broadening of the phase angle peak at lower frequencies to the growth of a passivating film on the metal surface,[29] which is in agreement with the respective polarization curves (Figure 2). The system has a capacitive behavior in the sense that a purely capacitive circuit would reach 90° at the lower frequency limit.[30] As reported in other works, the increase in the phase angle at lower frequencies comes along with a reduction in the electric double-layer capacitance of the system as a result of a film formation process.[31−33] At the intermediate inhibitor concentration of 5 mM (Figure 5c), the phase angle peak is greater compared to the control test and there is no clear trend with time, showing an oscillating behavior.

The stability of the protection after 24 h of immersion was studied with an additional impedance analysis (Figure 6). The Nyquist diagram still presents two capacitive arcs, where the low-frequency semicircle increases with inhibitor concentration following the same trend observed after 2 h of immersion (Figure 3). The impedance plot (Figure 6b) shows that the inhibitor has a major contribution to the corroding areas of the metal surface, causing an increase in the low-frequency impedance at higher inhibitor concentrations. SEM analysis supports this observation, showing the presence of a porous matrix on the localized corrosion region of the metal surface after inhibitor interaction (Figure 7c). The plot also includes the impedance data for the samples after 2 h of immersion (+ symbol). It is observed that there is no significant difference in the low-frequency impedance for 2 and 24 h of immersion. For the control test and in the case of the samples immersed in the inhibitor solution, there is a slight increase in their low-frequency impedance. The high-frequency impedance is not affected by the inhibitor or the immersion time, which is consistent with the polarization data that shows that the shape of the cathodic branch is invariable with inhibitor addition. Regarding the phase angle (Figure 6c), there is an increase and broadening of the low-frequency peak with higher inhibitor concentrations, reflecting a decrease in the electric double-layer capacitance of the system along with a deposition process.[28] The immersion time does not considerably affect the phase angle profiles for the sample immersed in the control and 2.5 mM inhibitor concentrations; however, at 5 mM inhibitor concentration, the protection improves after 24 h, decreasing the gap between the phase angle profiles for 5 and 10 mM inhibitor concentrations. In the case of the 10 mM inhibitor concentration, the phase angle peak turns into a

https://dx.doi.org/10.1021/acsomega.0c04733
ACS Omega 2021, 6, 1941−1952

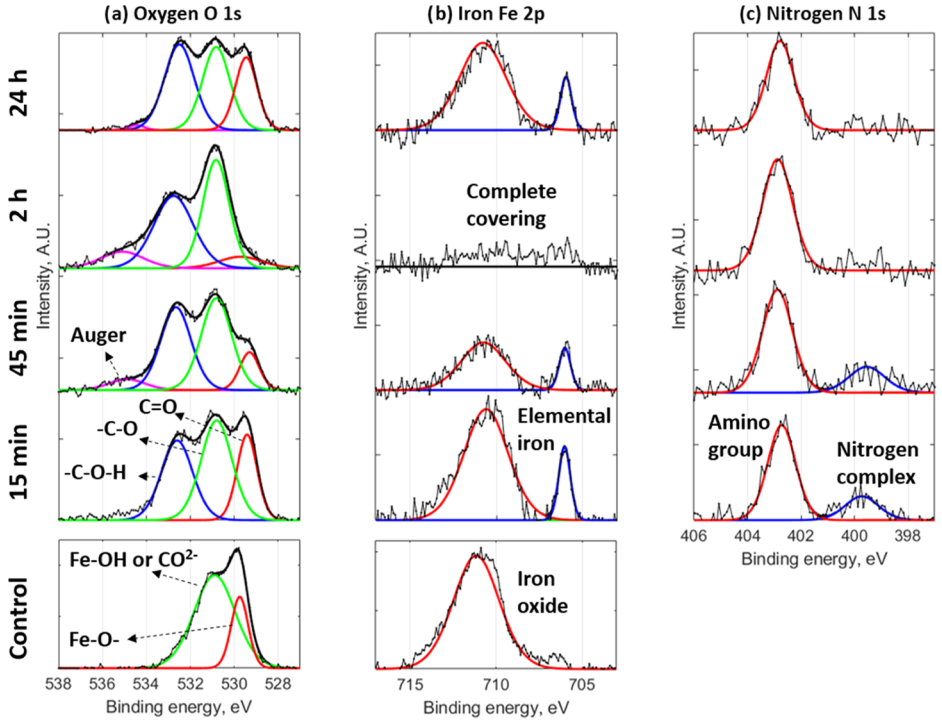

Figure 8. High-resolution XPS with deconvolution analysis of mild steel after 45 min of immersion in a 0.01 M NaCl control solution and various immersion times for 0.01 M NaCl + 10 mM CTA-4OHcinn solution for oxygen (a), iron (b), and nitrogen (c).

plateau, which is also related to the stability and improved protection of the film after 24 h of immersion.

The EIS data obtained after 24 h of immersion is fitted using the same equivalent circuit proposed for the analysis after 2 h of immersion (Figure 3b,c). The reason for using the same model is that the shape of the EIS spectra did not change considerably with the immersion time (e.g., the Nyquist plot still presents two capacitive loops after 24 h of immersion). The fitting parameters are shown in Table 2 enclosed in parenthesis and follow the same trend observed for the parameters obtained after 2 h of immersion. R_s, R_{pore}, $C_{ox/film}$, CPE_{EDL}, and α do not vary considerably with the immersion time. However, it is noticed that the charge-transfer resistance, R_{CT}, decreases for the sample after 24 h of immersion in the control solution, indicating the continuous deterioration of the metal surface as a result of corrosion, which agrees with its respective SEM image (Figure 7a). Conversely, for the samples immersed in different inhibitor solutions, the difference between the R_{CT} after 2 and 24 h of immersion increases as the inhibitor concentration increases. It should be clarified that the R_{CT} obtained for the sample after 24 h of immersion in the 10 mM inhibitor solution could be an artifact due to being related to the choice of the equivalent circuit model, resulting in the highest standard deviation (S^2) compared to the other cases; however, the trend is still valid, showing that the protection improves after 24 h of immersion.

The SEM images of the samples immersed for 24 h in the control and concentrated inhibitor solutions are shown in Figure 7. The sample immersed in the 0.01 M NaCl control solution (Figure 7a) shows an etched surface, where heterogeneous metal dissolution has occurred, leaving high relief zones. Cui et al. showed that pits were predominantly initiated in areas adjacent to carbon-rich phases, i.e., cementite in carbon steel immersed in chloride solutions.[34] In the case of the sample immersed in the 10 mM inhibitor solution, while the vast majority of the surface showed no damage (Figure 7c inset), the SEM image in Figure 8b shows the remains of a cap on the defective zone, which might be related to the buildup of molecular hydrogen due to early pitting corrosion.[35] The threadlike filaments around the defect observed in the same image are characteristic of filiform corrosion that indicate the presence of a dense film on the bulk of the surface, which blocks chloride attack across the interface and so its diffusion starts in the defective zone, extending below the film. The respective EDS map (Figure 7d) confirms this diffusion mechanism by showing a high chloride concentration at the fingertips of the filiform structure. Higher magnification of the defective zone on the metal surface after inhibitor interaction (Figure 7c) shows the formation of a porous matrix in the center. EDS analysis shows that this porous matrix is mostly composed of iron and oxygen, while the surrounding region has significant carbon content (see the Supporting Information).

Compositional analysis on the surface was undertaken by XPS to identify surface interactions and traces of the inhibitor compound. Table 3 shows the elemental analysis of the metal surfaces following immersion in the control solution for 45 min and the 10 mM inhibitor solution for 15 min, 45 min, 2 h, and 24 h. It is noted that the carbon content on the metal surface is higher for the samples immersed in the inhibitor solution compared to the control test. In addition, the oxygen, iron, and carbon contents of the samples immersed in the inhibitor solution reached a steady value after 45 min of immersion. This equilibration time is consistent with the lower-impedance window of 50 min reported in the impedance analysis (Figure 4d). Blin et al. proposed that film formation is conditioned by iron ions dissolved at the early stage of pitting corrosion.[9] The iron signal disappeared after 45 min and reappeared after 24 h. The disappearance of the iron signal after 45 min indicates the formation of a relatively dense, uniform film that does not

https://dx.doi.org/10.1021/acsomega.0c04733
ACS Omega 2021, 6, 1941−1952

Table 3. Elemental XPS Analysis for Mild Steel Immersed in a 0.01 M NaCl Control Solution and a 0.01 M NaCl + 10 mM CTA-4OHcinn Solution for Different Times

	oxygen %A	iron %A	carbon %A	nitrogen %A
control, 0.01 M NaCl after 45 min of immersion	39.1	7.4	53.5	0.0
0.01 NaCl + 10 mM CTA-4OHcinn solution after 15 min of immersion	15.0	0.8	81.2	2.3
0.01 NaCl + 10 mM CTA-4OHcinn solution after 45 min of immersion	11.5	0.0	84.1	1.9
0.01 NaCl + 10 mM CTA-4OHcinn solution after 2 h of immersion	10.9	0.0	84.7	1.1
0.01 NaCl + 10 mM CTA-4OHcinn solution after 24 h of immersion	12.1	0.6	83.5	1.9

contain iron over the surface. XPS analysis also reveals nitrogen in the sample surface after inhibitor interaction, which comes from the quaternary ammonium group of the cetrimonium cation (Figure 1).

Figure 8 shows the high-resolution XPS spectra for oxygen, iron, and nitrogen for the sample immersed at the same conditions as shown in Table 3. The spectrum of oxygen for the control test (Figure 8a) consists of two peaks at 529.7 and 530.9 eV (red and green lines, respectively). The first can be related to iron oxide and the second might correspond to an iron hydroxyl group (−OH) chemisorbed on the metal surface.[36] The latter peak (530.9 eV) can also reflect the presence of carbonates (CO^{2-}), which is consistent with the significant carbon content in the control, around 54% (Table 3). When the coupon is immersed in the inhibitor solution, a third oxygen peak emerges at 532.7 eV (blue line), which might be related to a hydroxyl group bonded to an aromatic ring in the para position,[37] therefore corresponding to the coumarate anion (Figure 1). Also, it is noticed that the 529.7 eV peak that was attributed in the control test to the presence of iron oxide can also be related to the carboxylate moiety of the coumarate anion in the case of the samples immersed in the inhibitor solution. Nevertheless, although the carboxylate group and the iron oxide have a similar binding energy, the intensity of the carboxylate is lower compared to the other two peaks.[38] In addition, there is a slight shift to lower binding energies of the carboxylate peaks, in the sample immersed in the inhibitor solution, compared to the iron oxide peak in the control test at 529.7 eV. This is consistent with the XPS analysis on cerium cinnamate powder, done by Shi et al.,[38] which showed two peaks at 529.6 and 531 eV attributed to the presence of a carbon−oxygen double bond (C═O) and a single carbon−oxygen bond (−C−O−), respectively. However, no peak was found around 532.7 eV due to the absence of a para-substituted hydroxyl in the cinnamate anion. The three peaks observed in this work for the sample immersed in the inhibitor solution at 529.7, 530.9, and 532.7 eV are consistent with the binding energy peaks found by Nam et al. at 529.8, 531.4, and 532.9 eV, after immersion of steel in praseodymium 4-hydroxycinnamate with NaCl solution.[6] The intensity of the red peak at 529.7 eV decreases with the immersion time, reaching a minimum after 2 h of immersion. This is consistent with the adsorption of the inhibitor on the metal surface, blocking the native oxide layer. However, after 24 h of immersion, the intensity of this peak increases again, which might be attributed to the formation of the porous oxide matrix observed in the metal surface (Figure 7c).

For the iron analysis (Figure 8b), the peak at 711.1 eV in the control test indicates the presence of Fe_2O_3, FeOOH, or $FeCO_3$, as indicated in the XPS spectrum of the oxygen (Figure 8a). When the sample was immersed in the inhibitor solution, the amount of iron present gradually decreased and was not detected after 2 h of immersion. This is consistent with the early plateau found in the impedance analysis (Figure 4d), and it could reflect an initial adsorption process of the inhibitor on the metal surface. As this film forms and covers the whole surface, the Fe signal disappears, corresponding to an increase in impedance seen in Figure 4d after 50 min. The Fe spectrum also shows a second peak at 706 eV that corresponds to elemental iron, which might indicate the growth of a heterogeneous film on the metal surface, leaving some active regions poorly covered to emit elemental iron signals. Eventually, after 2 h, the underlying Fe is not detected due to significant film deposition. We can also see from the disappearance of the Fe signal that the protective film does not contain Fe or Fe oxides/hydroxides. Similar to the oxygen spectrum, after 24 h of immersion, the iron signal appears again, which could be related to the emergence of the porous oxide matrix on the defective region (Figure 7c). This is likely due to ongoing Cl diffusion, particularly at the initially localized corrosion areas leading to filiform-type corrosion and the emergence of the porous oxide film observed in the SEM images.

Regarding the nitrogen analysis (Figure 8c), two peaks appear at 399.7 and 402.7 eV after inhibitor interaction. The high-intensity peak at 402.7 eV can be related to the amino group of the cetrimonium cation, which is present at all immersion times, as shown in Table 3. The low-intensity peak at 399.7 eV might be related to a nitrogen complex formed due

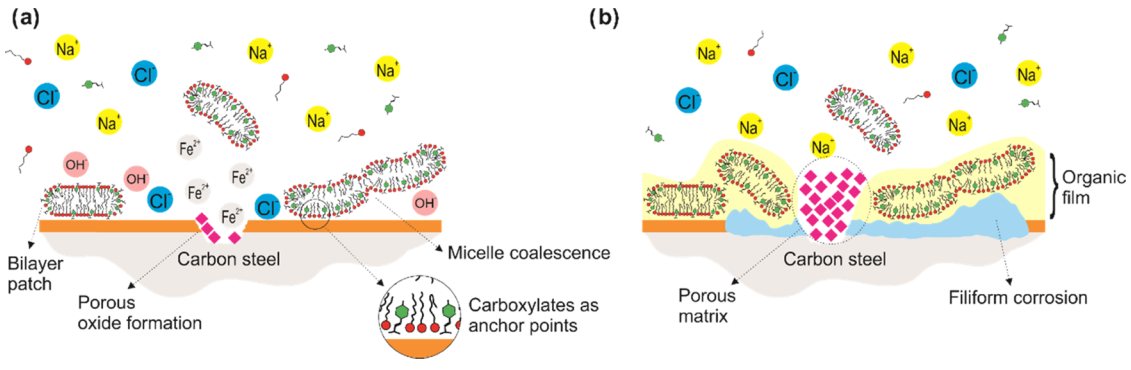

Figure 9. Proposed mechanism of interaction between the inhibitor CTA-4OHcinn and the metal surface in NaCl solution.

https://dx.doi.org/10.1021/acsomega.0c04733
ACS Omega 2021, 6, 1941−1952

to the initial interaction between the products released by initial pitting and the cetrimonium cations. Zhang et al. related the C-N and Fe-N groups of a triazole inhibitor to the binding energies 398.9 and 400 eV, respectively.[39] As the film builds up and there is no longer any Fe present at the surface, this peak disappears.

Figure 9 shows a schematic of the proposed mechanism that explains the interaction between the CTA-4OHcinn micelles, as reported by Ghorbani et al.,[18] and the metal surface. Initially, the inhibitor confers a moderate protection to the metal surface, but some localized corrosion can still occur (Figure 9a). This is consistent with the work of Ghorbani who reported a narrower passivating potential after 30 min of immersion compared to the one observed in the present work after 24 h of immersion (Figure 2).[18] At this stage, the metal surface is partially covered with inhibitor molecules, as shown in the XPS analysis, and chloride ions reach the metal-active region, marking the onset of localized corrosion. As a result of the early localized corrosion process, the properties of the solution near the interface will differ from the bulk phase. For example, Fe^{2+} and OH^- ions, formed at the interface, could increase the ionic strength and create pH-segregated zones,[35] which in turn would promote micelle coalescence.[27,40] It is also noticed that the carboxylates might serve as anchor points for the inhibitor micelles approaching the oxide surface. Lin et al. reported that carboxylates could be adsorbed on the steel surface through their delocalized electron charge on the two oxygen atoms, and the presence of C=C bonds stabilizes this adsorption process.[41] Forsyth et al. proposed a complexation mechanism between rare-earth carboxylates and metal surfaces by which a Fe-carboxylate-RE film is formed, based on surface analysis and speciation studies.[42] As the micelle adsorption increases on the oxide surface, there is a reduction in the available cathodic sites around the pitting region. The absence of cathodic sites leads to a decrease in the current transfer at the defective zone and a porous oxide begins to fill the pitting region. The second stage (Figure 9b) shows the complete coverage of the metal surface by the inhibitor aggregates, which, based on the XPS spectrum of iron, occurs within the first 2 h of immersion. It is also shown that the leakage of chloride ions throughout the defective zone can result in filiform corrosion, which was revealed by the SEM images of the sample after inhibitor interaction. Eventually, an oxide porous matrix builds up on the defective zone, hindering the pitting corrosion, which agrees with XPS analysis that shows the occurrence of iron oxide after 24 h of immersion along with SEM imaging that revealed this oxide morphology.

CONCLUSIONS

The cationic surfactant CTA-4OHcinn is able to effectively inhibit the corrosion of AS1030 mild steel in 0.01 M NaCl solutions. Polarization tests show the affinity of the inhibitor to hinder anodic reactions on the metal surface and also develop a passivating layer at high inhibitor concentrations. Time-resolved EIS indicate the presence of an initial low-protection stage in the first 45 min of immersion, where the inhibitor is being adsorbed on the metal surface and there is some initial pitting. However, the pitting process is eventually shut down by the deposition of some porous material on the defective zones of the metal surface along with the formation of an organic surface layer, as revealed by SEM images. The newly formed inhibitor surface layer restricts chloride attack on the bulk of the metal surface. However, where there is defect in the film, diffusion of chloride can persist under the organic surface layer and lead to filiform corrosion, with high chloride deposits detected in the tip of the fingerlike structures. XPS analysis confirms inhibitor adsorption on the metal surface, detecting carboxylates and amine groups that come from the aromatic counterion 4-OH cinnamate and the cetrimonium cation, respectively. It also shows the kinetics of the surface deposition process, where iron signals gradually fade out with the immersion time and complete surface coverage is achieved after 2 h, supporting the initial inactivation window observed by time-resolved EIS. However, some regions might be poorly covered, where corrosion may eventually occur, resulting in the elemental iron signal returning after 24 h of immersion.

EIS analysis over the first 2 h of immersion shows that the inhibitor has a significant effect on the charge-transfer mechanism between the corroding regions of the metal surface and the electrolyte. Based on the proposed circuit model, the decrease in the electric double-layer constant phase element, along with the sharp increase in the charge-transfer resistance at higher inhibitor concentrations, indicates a deposition process on the corroding areas of the metal surface. This is in agreement with SEM images that show the deposition of a porous matrix on the localized corrosion region along with the formation of an organic layer and also with polarization tests that show that CTA-4OHcinn is an anodic inhibitor. Finally, the stability of the film after 24 h of immersion is confirmed by EIS analysis, showing no significant change in the impedance spectrum compared to the EIS data after 2 h of immersion. On the contrary, a slight increase in the impedance was observed, along with a broadening of the phase angle and a closer approach to 90°.

ASSOCIATED CONTENT

Supporting Information

The Supporting Information is available free of charge at https://pubs.acs.org/doi/10.1021/acsomega.0c04733.

Replica for potentiodynamic polarization tests, phase angle and Bode plot for mild steel immersed for 2 h in solution, time evolution of the Nyquist plot over the first 2 h of immersion, and EDS map of the porous matrix (PDF)

AUTHOR INFORMATION

Corresponding Authors

Maria Forsyth − *Institute for Frontier Materials, Deakin University, Burwood, Victoria 3125, Australia;* orcid.org/0000-0002-4273-8105; Email: maria.forsyth@deakin.edu.au

Anthony E. Somers − *Institute for Frontier Materials, Deakin University, Burwood, Victoria 3125, Australia;* orcid.org/0000-0002-0220-2904; Email: anthony.somers@deakin.edu.au

Authors

Jhonatan Soto Puelles − *Institute for Frontier Materials, Deakin University, Burwood, Victoria 3125, Australia*

Mahdi Ghorbani − *Institute for Frontier Materials, Deakin University, Burwood, Victoria 3125, Australia*

Ruhamah Yunis − *Institute for Frontier Materials, Deakin University, Burwood, Victoria 3125, Australia*

Laura L. Machuca − *Curtin Corrosion Centre, Curtin University, Bentley, Western Australia 6102, Australia*

https://dx.doi.org/10.1021/acsomega.0c04733
ACS Omega 2021, 6, 1941−1952

Herman Terryn − *Research Group of Electrochemical and Surface Engineering (SURF), Department of Materials and Chemistry, Vrije Universiteit Brussel, 1050 Brussels, Belgium;* orcid.org/0000-0003-2639-5496

Complete contact information is available at: https://pubs.acs.org/10.1021/acsomega.0c04733

Notes

The authors declare no competing financial interest.

■ ACKNOWLEDGMENTS

Authors acknowledge the Australian Research Council (ARC) Discovery Project funding (DP180101465). J.S.P., M.G., R.Y., M.F., and A.E.S. acknowledge the support of The Institute for Frontier Materials and Deakin University. J.S.P. thanks Dr. Rainier Catubig and Professor Bruce Hinton.

■ REFERENCES

(1) Forsyth, M.; Seter, M.; Tan, M.; Hinton, B. Recent developments in corrosion inhibitors based on rare earth metal compounds. *Corros. Eng., Sci. Technol.* **2014**, *49*, 130−135.

(2) Mercer, A. D. In *5th European Symposium on 'Corrosion Inhibitors'*, Proceedings of the 107th Manifestation of the European Federation of Corrosion, Ferrara, Italy, 15−19 September 198, Volume 3, 1980.

(3) Hinton, B. W.; Arnott, D. R.; Ryan, N. E. Inhibition of aluminum alloy corrosion by cerous cations. *Metal Forum* **1984**, 221.

(4) Behrouzvaziri, M.; Hinton, B. R. W.; Forsyth, M. The effects of concentration and structure of lanthanum and cerium based inhibitors on the corrosion rate of mild steel in chloride solutions. In *Corrosion and Prevention 2008*; Australasian Corrosion Association: Wellington, 2008.

(5) Behrouzvaziri, M. Inhibition of Corrosion on Steel using New Rare Earth Carboxylate Compounds. Monash University, Doctoral Dissertation, 2009.

(6) Nam, N. D.; Somers, A.; Mathesh, M.; Seter, M.; Hinton, B.; Forsyth, M.; Tan, M. The behaviour of praseodymium 4-hydroxycinnamate as an inhibitor for carbon dioxide corrosion and oxygen corrosion of steel in NaCl solutions. *Corros. Sci.* **2014**, *80*, No. 128.

(7) Seter, M.; Girard, G.; Lee, W. W.; Deacon, G.; Junk, P.; Hinton, B.; Forsyth, M. The influence of organic structure and rare earth metal cation on the corrosion efficiency observed on AS1020 steel compared with La $(4OHCin)_3$. *AIMS Mater. Sci.* **2015**, *2*, 1−15.

(8) Nam, N. D.; Van Hien, P.; Hoai, N. T.; Thu, V. T. H. A study on the mixed corrosion inhibitor with a dominant cathodic inhibitor for mild steel in aqueous chloride solution. *J. Taiwan Inst. Chem. Eng.* **2018**, *91*, 556−569.

(9) Blin, F.; Leary, S. G.; Deacon, G. B.; Junk, P. C.; Forsyth, M. The nature of the surface film on steel treated with cerium and lanthanum cinnamate based corrosion inhibitors. *Corros. Sci.* **2006**, *48*, 404−419.

(10) Nam, N.; Ha, P.; Anh, H.; Hoai, N.; Hien, P. Role of hydroxyl group in cerium hydroxycinnamate on corrosion inhibition of mild steel in 0.6 M NaCl solution. *J. Saudi Chem. Soc.* **2019**, *23*, No. 30.

(11) Nam, N. D.; Panaitescu, C.; Tan, M.; Forsyth, M.; Hinton, B. An interaction between praseodymium 4-hydroxycinnamate with AS1020 and X65 steel microstructures in carbon dioxide environment. *J. Electrochem. Soc.* **2018**, *165*, C50.

(12) Hien, P. V.; Vu, N.; Thu, V.; Somers, A.; Nam, N. Study of yttrium 4-nitrocinnamate to promote surface interactions with AS1020 steel. *Appl. Surf. Sci.* **2017**, *412*, No. 464.

(13) Chong, A. L.; Mardel, J. I.; MacFarlane, D. R.; Forsyth, M.; Somers, A. E. Synergistic corrosion inhibition of mild steel in aqueous chloride solutions by an imidazolinium carboxylate salt. *ACS Sustainable Chem. Eng.* **2016**, *4*, No. 1746.

(14) Seter, M.; Thomson, M. J.; Chong, A.; MacFarlane, D. R.; Forsyth, M. Cetrimonium nalidixate as a multifunctional inhibitor to combat biofilm formation and microbiologically influenced corrosion. *Aust. J. Chem.* **2013**, *66*, No. 921.

(15) Vinarov, Z.; Katev, V.; Radeva, D.; Tcholakova, S.; Denkov, N. Micellar solubilization of poorly water-soluble drugs: effect of surfactant and solubilizate molecular structure. *Drug Dev. Ind. Pharm.* **2018**, *44*, 677−686.

(16) Yan, H.; Han, Z.; Li, K.; Li, G.; Wei, X. Molecular dynamics simulation of the pH-induced structural transitions in CTAB/NaSal solution. *Langmuir* **2018**, *34*, No. 351.

(17) Lin, Z.; Cai, J.; Scriven, L.; Davis, H. Spherical-to-wormlike micelle transition in CTAB solutions. *J. Phys. Chem. A* **1994**, *98*, 5984−5993.

(18) Ghorbani, M.; Puelles, J.; Forsyth, M.; Catubig, R.; Ackland, L.; Machuca, L.; Terryn, H.; Somers, A. Corrosion inhibition of mild steel by cetrimonium trans-4-hydroxy cinnamate; entrapment and delivery of the anion inhibitor through speciation and micellar formation. *J. Phys. Chem. Lett.* **2020**, *11*, 9886−9892.

(19) Frankel, G. Pitting corrosion of metals a review of the critical factors. *J. Electrochem. Soc.* **1998**, *145*, 2186−2198.

(20) Jones, D. A. *Principles and Prevention of Corrosion*, 2nd ed.; Upper Saddler River: Prentice-Hall, 1996; pp 75−100.

(21) Macdonald, J. R.; Barsoukov, E. *Impedance Spectroscopy: Theory, Experiment, and Applications*, 2nd ed.; John Wiley & Sons: New Jersey, 2005; pp 1−13.

(22) Gomes, M. P.; Costa, I.; Pébère, N.; Rossi, J. L.; Tribollet, B.; Vivier, V. On the corrosion mechanism of Mg investigated by electrochemical impedance spectroscopy. *Electrochim. Acta* **2019**, *306*, No. 61.

(23) Hirschorn, B.; Orazem, M. E.; Tribollet, B.; Vivier, V.; Frateur, I.; Musiani, M. Constant-phase-element behavior caused by resistivity distributions in films: II. Applications. *J. Electrochem. Soc.* **2010**, *157*, C458.

(24) Dagdag, O.; Safi, Z.; Hsissou, R.; Erramli, H.; El Bouchti, M.; Wazzan, N.; Guo, L.; Verma, C.; Ebenso, E.; El Harfi, A. Epoxy pre-polymers as new and effective materials for corrosion inhibition of carbon steel in acidic medium: Computational and experimental studies. *Sci. Rep.* **2019**, *9*, No. 7065.

(25) Feng, P.; Wan, K.; Cai, G.; Yang, L.; Li, Y. Synergistic protective effect of carboxymethyl chitosan and cathodic protection of X70 pipeline steel in seawater. *RSC Adv.* **2017**, *7*, No. 3419.

(26) Boudellioua, H.; Hamlaoui, Y.; Tifouti, L.; Pedraza, F. Effects of polyethylene glycol (PEG) on the corrosion inhibition of mild steel by cerium nitrate in chloride solution. *Appl. Surf. Sci.* **2019**, *473*, No. 449.

(27) Sangwai, A. V.; Sureshkumar, R. Binary interactions and salt-induced coalescence of spherical micelles of cationic surfactants from molecular dynamics simulations. *Langmuir* **2012**, *28*, No. 1127.

(28) Duan, H.; Du, K.; Yan, C.; Wang, F. Electrochemical corrosion behavior of composite coatings of sealed MAO film on magnesium alloy AZ91D. *Electrochim. Acta* **2006**, *51*, No. 2898.

(29) Ye, C.-Q.; Hu, R.-G.; Dong, S.-G.; Zhang, X.-J.; Hou, R.-Q.; Du, R.-G.; Lin, C.-J.; Pan, J.-S. EIS analysis on chloride-induced corrosion behavior of reinforcement steel in simulated carbonated concrete pore solutions. *J. Electroanal. Chem.* **2013**, *688*, No. 275.

(30) Floyd, T. L.; Buchla, D. *Electronics Fundamentals: Circuits, Devices & Applications*, 8th ed.; Pearson Education Limited: Harlow, 2014; pp 459−465.

(31) Sliem, M. H.; Afifi, M.; Radwan, A. B.; Fayyad, E. M.; Shibl, M. F.; Heakal, F. E.-T.; Abdullah, A. M. AEO7 surfactant as an eco-friendly corrosion inhibitor for carbon steel in HCl solution. *Sci. Rep.* **2019**, *9*, No. 2319.

(32) Visser, P.; Terryn, H.; Mol, J. M. On the importance of irreversibility of corrosion inhibitors for active coating protection of AA2024-T3. *Corros. Sci.* **2018**, *140*, No. 272.

(33) El-Hajjaji, F.; Messali, M.; Aljuhani, A.; Aouad, M.; Hammouti, B.; Belghiti, M.; Chauhan, D.; Quraishi, M. Pyridazinium-based ionic liquids as novel and green corrosion inhibitors of carbon steel in acid medium: electrochemical and molecular dynamics simulation studies. *J. Mol. Liq.* **2018**, *249*, No. 997.

(34) Cui, N.; Qiao, L.; Luo, J.; Chiovelli, S. Pitting of carbon steel with banded microstructures in chloride solutions. *Br. Corros. J.* **2000**, *35*, 210−215.
(35) Wranglén, G. *An Introduction to Corrosion and Protection of Metals. Anti-Corrosion Methods Materials and Corrosion*; Springer: Netherlands, 1972; pp 55−60.
(36) Chauhan, P.; Gadiyar, H.; Krishnan, R. X-ray photoelectron spectroscopy for surface film analysis in corrosion research. *Springer Ser. Solid-State Sci.* **1985**, *24*, No. 383.
(37) Fleutot, S.; Dupin, J.-C.; Renaudin, G.; Martinez, H. Intercalation and grafting of benzene derivatives into zinc−aluminum and copper−chromium layered double hydroxide hosts: an XPS monitoring study. *Phys. Chem. Chem. Phys.* **2011**, *13*, No. 17564.
(38) Shi, H.; Han, E.-H.; Liu, F. Corrosion protection of aluminium alloy 2024-T3 in 0.05 M NaCl by cerium cinnamate. *Corros. Sci.* **2011**, *53*, No. 2374.
(39) Zhang, Z.; Wang, F.; Liu, Y.; Wu, S.; Li, W.; Sun, W.; Guo, D.; Jiang, J. Molecule adsorption and corrosion mechanism of steel under protection of inhibitor in a simulated concrete solution with 3.5% NaCl. *RSC Adv.* **2018**, *8*, No. 20648.
(40) Davies, J.; Rideal, E. *Interfacial Phenomena*, 2nd ed.; Academic Press: New York, 1963; pp 60−75.
(41) Lin, B.; Zuo, Y. Corrosion inhibition of carboxylate inhibitors with different alkylene chain lengths on carbon steel in an alkaline solution. *RSC Adv.* **2019**, *9*, No. 7065.
(42) Forsyth, M.; Seter, M.; Hinton, B.; Deacon, G.; Junk, P. New 'green'corrosion inhibitors based on rare earth compounds. *Aust. J. Chem.* **2011**, *64*, No. 812.

https://dx.doi.org/10.1021/acsomega.0c04733
ACS Omega 2021, 6, 1941−1952